

RESEARCH ARTICLE

# A Functional Cancer Genomics Screen Identifies a Druggable Synthetic Lethal Interaction between *MSH3* and *PRKDC*

Felix Dietlein<sup>1</sup>, Lisa Thelen<sup>4</sup>, Mladen Jokic<sup>4</sup>, Ron D. Jachimowicz<sup>4</sup>, Laura Ivan<sup>4</sup>, Gero Knittel<sup>4</sup>, Uschi Leeser<sup>4</sup>, Johanna van Oers<sup>5</sup>, Winfried Edelmann<sup>5</sup>, Lukas C. Heukamp<sup>2</sup>, and H. Christian Reinhardt<sup>3,4</sup>

**ABSTRACT**

Here, we use a large-scale cell line-based approach to identify cancer cell-specific mutations that are associated with DNA-dependent protein kinase catalytic subunit (DNA-PKcs) dependence. For this purpose, we profiled the mutational landscape across 1,319 cancer-associated genes of 67 distinct cell lines and identified numerous genes involved in homologous recombination-mediated DNA repair, including *BRCA1*, *BRCA2*, *ATM*, *PAXIP*, and *RAD50*, as being associated with non-oncogene addiction to DNA-PKcs. Mutations in the mismatch repair gene *MSH3*, which have been reported to occur recurrently in numerous human cancer entities, emerged as the most significant predictors of DNA-PKcs addiction. Concordantly, DNA-PKcs inhibition robustly induced apoptosis in *MSH3*-mutant cell lines *in vitro* and displayed remarkable single-agent efficacy against *MSH3*-mutant tumors *in vivo*. Thus, we here identify a therapeutically actionable synthetic lethal interaction between *MSH3* and the non-homologous end joining kinase DNA-PKcs. Our observations recommend DNA-PKcs inhibition as a therapeutic concept for the treatment of human cancers displaying homologous recombination defects.

**SIGNIFICANCE:** We associate mutations in the *MSH3* gene, which are frequently detected in microsatellite-unstable colon cancer (~40%), with a therapeutic response to specific DNA-PKcs inhibitors. Because potent DNA-PKcs inhibitors are currently entering early clinical trials, we offer a novel opportunity to genetically stratify patients who may benefit from a DNA-PKcs-inhibitory therapy. *Cancer Discov*; 4(5); 592–605. © 2014 AACR.

See related commentary by Hemann, p. 516.

**INTRODUCTION**

In response to DNA damage, cells activate a complex signaling cascade to prevent further cell-cycle progression (1). Activation of this signaling pathway, which is commonly referred to as the DNA damage response (DDR), allows time for DNA repair, or, if the lesions are beyond repair capacity, leads to the induction of apoptosis (1). Mammalian cells have evolved at least five partially overlapping DNA repair pathways to correct various types of genotoxic lesions—mismatch repair (MMR), nucleotide-excision repair (NER), base-excision repair (BER), homologous recombination, and non-homologous end joining (NHEJ; ref. 2). MMR removes nucleotides that were mispaired during replication, as well as insertion and deletion loops, which result from slippage during the replication of repetitive sequences. The NER pathway is used to repair helix-distorting lesions, whereas small chemical modifications of bases are removed by the BER machinery (2).

Specifically in response to DNA double-strand breaks (DSB), mammalian cells use two distinct repair pathways. NHEJ is an

error-prone pathway that is preferentially used during early phases of the cell cycle, when no sister chromatid is available (3). During NHEJ, the noncatalytic subunits KU70 and KU80 form a heterodimer that binds to the free DNA ends and subsequently recruits the catalytic subunit DNA-PKcs (encoded by *PRKDC*). DNA-PKcs kinase activity is essential for XRCC4- and LIG4-mediated rejoining of the broken DNA ends during NHEJ (4). Homologous recombination, the second major DSB repair pathway, is largely restricted to the S- and G<sub>2</sub>-phases of the cell cycle, when a sister chromatid is available to serve as an intact template for DSB repair (5). One of the early events, necessary for completion of the homologous recombination process, is DSB end resection to create a single-stranded 3'-overhang, which becomes rapidly coated with the single-strand-binding protein replication protein A (RPA) and provides a substrate for activation of the proximal DDR kinase ATR (6). During the ensuing steps of the homologous recombination process, RPA is replaced by RAD51, which is recruited to ssDNA in a *BRCA1*/*BRCA2*/*PALB2*-dependent fashion (7). Once loaded onto ssDNA, RAD51 mediates the core reactions of the homologous recombination process, namely homology searching, strand exchange, and Holliday junction formation (5).

The homologous recombination pathway is indispensable for the maintenance of genomic integrity, and patients with heterozygous germline mutations in different homologous recombination genes display a massively increased risk for the development of cancer (7). Most notably, germline mutations in *BRCA1*, *BRCA2*, and *RAD51C* are associated with predisposition to breast and ovarian cancer (8, 9). Furthermore, numerous homologous recombination genes, including *BRCA1*, *BRCA2*, *ATM*, *CHEK2*, *RAD50*, *RAD51C*, and others, are recurrently somatically mutated in various different cancer entities (7).

Intriguingly, homologous recombination deficiency in *BRCA1*- or *BRCA2*-defective cells and tumors was recently shown

**Authors' Affiliations:** <sup>1</sup>Department of Translational Genomics; <sup>2</sup>Institute of Pathology; <sup>3</sup>Cologne Excellence Cluster on Cellular Stress Response in Aging-Associated Diseases, University of Cologne; <sup>4</sup>Department of Internal Medicine, University Hospital of Cologne, Cologne, Germany; and <sup>5</sup>Michael F. Price Center, Albert Einstein College of Medicine, Bronx, New York

**Note:** Supplementary data for this article are available at Cancer Discovery Online (<http://cancerdiscovery.aacrjournals.org/>).

F. Dietlein and L. Thelen contributed equally to this work.

**Corresponding Author:** H. Christian Reinhardt, Department of Internal Medicine, University Hospital of Cologne, Kerpener Street 62, 50931 Cologne, Germany. Phone: 49-221-478-96701; Fax: 49-221-478-97835; E-mail: christian.reinhardt@uk-koeln.de

**doi:** 10.1158/2159-8290.CD-13-0907

©2014 American Association for Cancer Research.

to represent an actionable alteration in cancer. Specifically, a series of recent studies reported a synthetic lethal interaction between *PARP1* and the high-penetrance breast and ovarian cancer susceptibility genes *BRCA1* and *BRCA2* (10, 11). In addition, we and others have recently identified a druggable synthetic lethal interaction between the homologous recombination gene *ATM* and the NHEJ kinase gene *PRKDC* (12–14). Here, we propose that it is the homologous recombination defect that is responsible for the robust non-oncogene addiction to DNA-PKcs that we had previously observed in *ATM*-mutant cells and tumors (14). Thus, the aim of this study was to compile a systematic classification of the most frequent mutations in cancer, which are most likely to be associated with an actionable DNA-PKcs addiction. To this end, we used a combined genomic and chemical vulnerability analysis of 94 cancer cell lines and examined the effect of mutations in 1,319 cancer-associated genes on DNA-PKcs dependence. Furthermore, we functionally confirmed the most striking associations that we identified in high-throughput screening and deciphered mechanisms that might rationalize these effects. Finally, we provide a detailed examination of our novel therapeutic strategies *in vivo*.

## RESULTS

### Activity Profile of KU60648 in a Large Panel of Genomically Annotated Cancer Cell Lines

To identify genomic aberrations that are associated with non-oncogene addiction to the NHEJ kinase DNA-PKcs, we screened the specific DNA-PKcs inhibitor KU60648 ( $IC_{50} = 19 \text{ nmol/L}$ ; ref. 15) against a panel of 94 genomically well-annotated cancer cell lines (Supplementary Table S1), which covered a broad spectrum of cancer entities, histologic subtypes (Supplementary Fig. S1A, inset), and cancer-associated genomic aberrations (Fig. 1A and B). We used the *BRD4-NUT*-fused cell line HCC2429 as a positive control (Fig. 1A and Supplementary Table S1), for which we had recognized addiction to DNA-PKcs in follow-up experiments of a previous study (14). Conversely, A375 and A549 cells, which we had previously shown to be resistant to the DNA-PKcs inhibitor KU60648, were included to benchmark DNA-PKcs independence (14). Cell viability was assessed using high-throughput luminescence-based measurements of relative cellular ATP content by CellTiter-Glo assay.

To identify genomic aberrations that are associated with DNA-PKcs addiction, we systematically linked compound activity in 67 cell lines to mutation status of 1,319 cancer-associated genes (Fig. 1B and C; Supplementary Figs. S1 and S2; refs. 16–20). We analyzed Hill coefficients and nearest-neighbor distances to identify 400 nmol/L as the threshold concentration for KU60648 sensitivity (Supplementary Fig. S1B). We used this threshold to classify cell lines into KU60648-sensitive and -resistant groups. Comparing for each gene its mutation frequency between the two cohorts (Fisher exact test), we identified 121 genes, for which mutations significantly ( $P < 0.05$ ) coclustered with KU60648 sensitivity, as well as *MAP3K1* mutations, which emerged as the only significant ( $P = 0.048$ ) genomic marker predicting KU60648 resistance (Fig. 1B). We note that mutations in *PRKDC* were strongly associated with KU60648 resistance, suggesting that the compound was indeed targeting DNA-PKcs.

We initially hypothesized that NHEJ abrogation through DNA-PKcs inhibition should selectively eradicate homologous recombination-defective cells. Consistent with this notion, mutations in the homologous recombination genes *BRCA2* ( $P = 1.06 \times 10^{-4}$ ), *RAD50* ( $P = 3.99 \times 10^{-3}$ ), *CHEK2* ( $P = 5.97 \times 10^{-3}$ ), and *PAXIP* ( $P = 1.33 \times 10^{-4}$ , encoding PTIP), as well as the Fanconi anemia pathway component *FANCD2* ( $P = 5.97 \times 10^{-3}$ ), emerged as lesions that significantly coclustered with KU60648 sensitivity. Mutations in different components of the PTIP-MLL3-MLL4 complex, which plays a critical role in RAG-mediated cleavage and repair during V(D)J recombination (21), as well as homologous recombination-mediated DSB repair (22), emerged as highly significant determinants of DNA-PKcs dependence (Fig. 1B). Specifically, frameshift mutations in *MLL3* (encoding the PTIP-interacting protein MLL3;  $P = 9.32 \times 10^{-4}$ ) were identified as significant predictors for non-oncogene addiction to the NHEJ kinase DNA-PKcs. Furthermore, mutations in *ATM* and *BRCA1* were also associated with KU60648 sensitivity (Supplementary Fig. S2). Although displaying strong effects ( $GI_{50}$  ratio  $\geq 3.5$ ), these associations did not meet significance criteria, either due to the low mutation frequency of these genes in the examined cancer lines (e.g., *BRCA1*;  $n = 3$ ) or due to dissimilar effects on compound activity depending on the respective mutation type (e.g., *ATM*); exclusively frameshift mutations of the latter coclustered significantly with compound activity (Supplementary Fig. S2). In agreement with our initial hypothesis, a Gene Ontology (GO)-based analysis (23) revealed that disabling mutations in DNA repair genes were significantly ( $P = 2.98 \times 10^{-12}$ ) enriched in DNA-PKcs inhibitor-sensitive cell lines (Fig. 1A, inset). In particular, we observed an accumulation of homologous recombination genes, for which mutations were significantly associated with KU60648 sensitivity. The initial steps of the homologous recombination pathway can be arbitrarily clustered into three distinct processes, namely focus nucleation, DSB resection, and RAD51 loading (Fig. 1C); our screen revealed mutations in critical components of each process (Fig. 1C). These data suggest that homologous recombination deficiency in general represents a cancer-associated condition that displays synthetic lethality with the NHEJ kinase DNA-PKcs.

To our surprise, mutations in the MMR gene *MSH3* ( $P = 9.53 \times 10^{-4}$ ) emerged among the most significant predictors of compound activity (Fig. 1B). Further analysis revealed that *MSH3* mutations gained strongly in significance ( $P = 7.43 \times 10^{-6}$ ) and activity effect ( $GI_{50}$  ratio, 5.3) when restricted to protein structure-damaging microdeletions in the two longest mononucleotide/trinucleotide repeat sequences of the *MSH3* coding sequence (Fig. 1A and B and Supplementary Figs. S2 and S3A). Intriguingly, frameshift mutations in *A<sub>8</sub>* stretches occur frequently as somatic alterations of *MSH3* in microsatellite-unstable (MSI) colorectal cancer (24–27). Concordantly, we detected such mutations in our cancer cell line panel; 10 of 67 cell lines displayed microdeletions in the two longest mononucleotide/trinucleotide repeat sequences (Fig. 1A and Supplementary Fig. S3A). Together, our observations strongly suggest that DNA-PKcs inhibition might emerge as a novel therapeutic principle for the targeted treatment of *MSH3*-defective cancer.

In our initial screen, we noticed that only two of a total of three *BRCA1*-mutant cell lines were classified as KU60648-sensitive (H1838 and H1563). To molecularly dissect this diverse

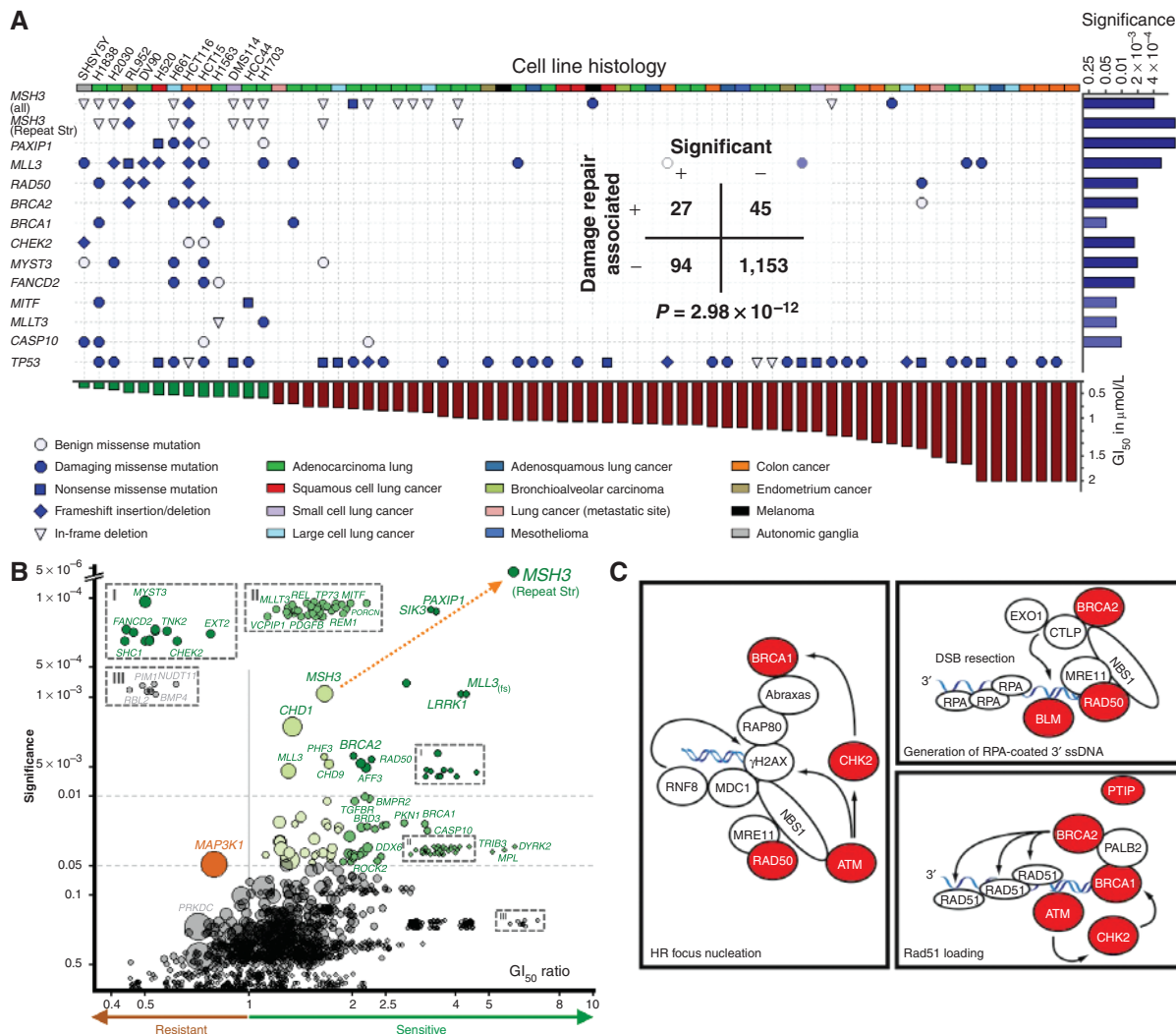


**Figure 1.** Biologic activity of the DNA-PKcs inhibitor KU60648 associates with mutations in DNA repair genes. **A**, GI<sub>50</sub>s of the DNA-PKcs inhibitor KU60648 are plotted for 67 cancer lines (bottom). Aberration frequencies (Cancer Cell Line Encyclopedia database) of 13 genes in KU60648-sensitive (GI<sub>50</sub> < 400 nmol/L; green) versus KU60648-resistant (red) cell lines are compared by the Fisher exact test (right). For each cell line, the corresponding histology (top), as well as the mutational status for 13 selected genes, is shown (grid plot). Inset, GO term-based analysis of damage-associated genes by the Fisher exact test. **B**, volcano plot representation of a systematic association of mutations in 1,319 genes with DNA-PKcs inhibitor sensitivity (KU60648) across a panel of 94 cancer cell lines. For each gene, significance (Fisher exact test, y-axis) is plotted against the ratio of average GI<sub>50</sub> values of mutant versus wild-type cell lines (y-axis). Circle sizes are proportional to the number of mutant cell lines included in the screen. Insets I–III are magnified views of ratio-sensitivity associations. **C**, functional clustering of sensitivity-associated mutations into the homologous recombination (HR)-mediated DNA repair pathway. Protein interactions are represented schematically; alterations, which are associated with DNA-PKcs inhibitor sensitivity, are highlighted in red. Str, short tandem repeat.

pattern of compound sensitivity, we subjected the *BRCA1*<sup>mut</sup> cell lines H2347, H1563, and H1838 to Sanger sequencing of all 23 *BRCA1* exons (Supplementary Fig. S3B–S3D) and found that only the H1563 cell line carried homozygous *BRCA1* mutations. Intriguingly, KU60648-sensitive H1838 cells did not show homozygous *BRCA1* mutations. However, they carried an *MSH3* mutation (Fig. 1A), which likely rationalizes their KU60648 sensitivity.

### DNA-PKcs Inhibition Induces Apoptosis in *MSH3*-Mutant Cells

The CellTiter-Glo assays revealed that *MSH3*-mutant cell lines displayed a robust DNA-PKcs inhibitor response

( $P_{\max} = 7.81 \times 10^{-6}$ ,  $t$  test; Supplementary Fig. S1C). To address the characteristics of the apparent reduction of cell viability that we observed in *MSH3*-mutant cells, we next quantified KU60648-induced cell-cycle arrest and apoptosis using immunoblotting (Fig. 2A) and flow cytometry (Fig. 2B and Supplementary Fig. S4). To this end, cell-cycle profiles of a panel of six sensitive (HCC44, H1838, H1703, H2030, H1563, and HCC2429) and three resistant (H2347, HCC1359, and H1915) cell lines were longitudinally monitored at seven distinct time points under 1  $\mu$ mol/L exposure of KU60648 (0, 6, 12, 24, 48, 72, and 96 hours). H1563 cells carrying homozygous protein-damaging *BRCA1* mutations (Supplementary Fig. S3B–S3D), as well as HCC2429 cells that

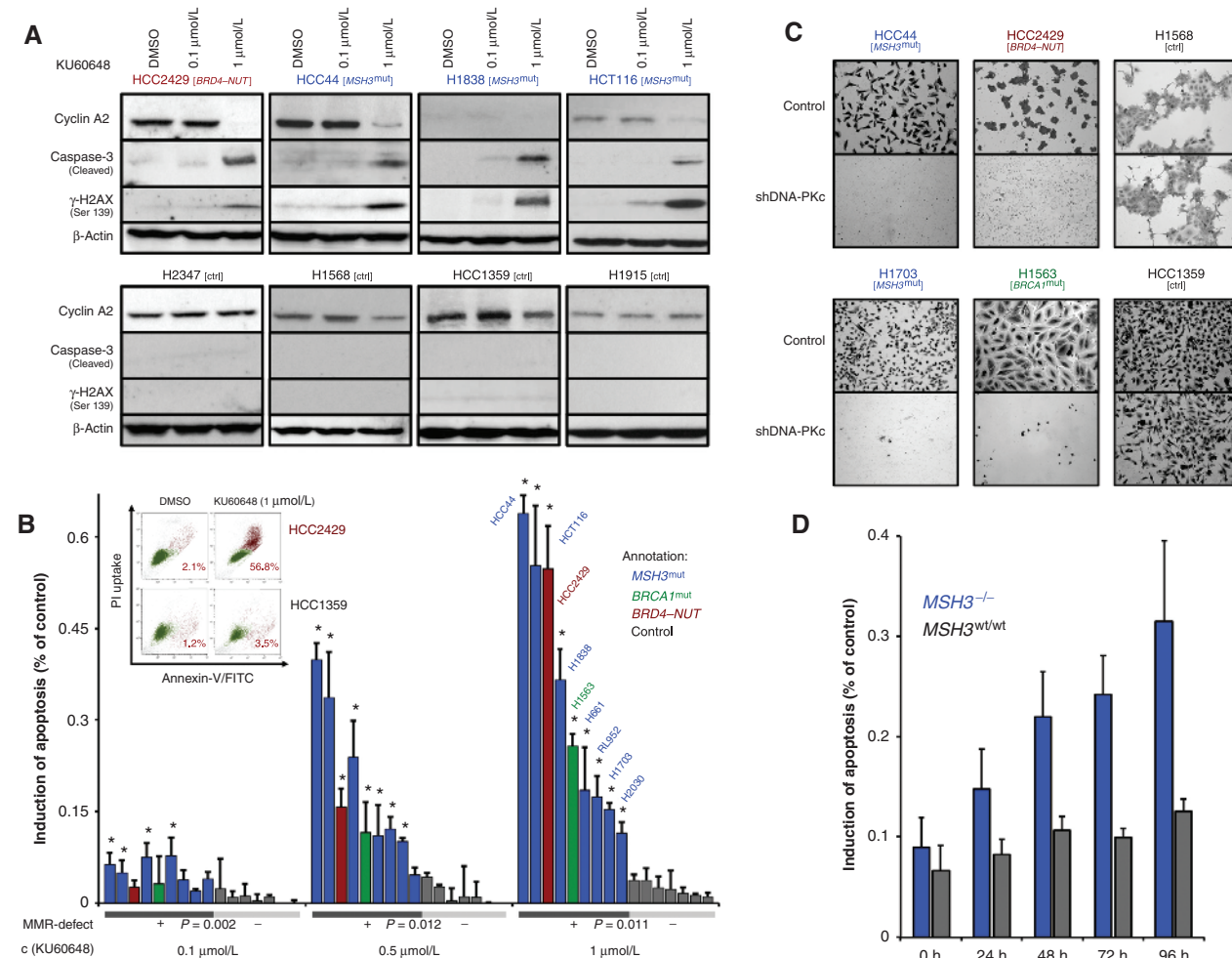


**Figure 2.** Functional and genetic validation of KU60648 activity across *MSH3*-mutated and *Msh3*-deficient cell lines. **A**, induction of apoptosis after 72-hour exposure to KU60648 (0, 0.1, 0.5, and 1 μmol/L) in 16 cancer lines was assessed by flow cytometry (annexin-V/PI double-positive populations). Error bars, SDs of three independent experiments; significance was calculated by t test. \*, values that are significantly superior to control. Inset, exemplary dot plots of annexin-V/PI double-positive apoptotic cell populations. **B**, protein expression of cleaved caspase-3, cyclin A2, γ-H2AX, and β-actin was assessed in HCC2429 [BRD4-NUT], HCC44 [MSH3mut], H1838 [MSH3mut], HCT116 [MSH3mut], H2347 [ctrl], H1568 [ctrl], HCC1359 [ctrl], and H1915 [ctrl] cells after 48-hour treatment with the DNA-PKcs inhibitor KU60648 (0, 0.1, and 1 μmol/L) by immunoblotting. Of note, not all bands were detected at the same membrane due to overlapping protein sizes. **C**, representative morphology ( $\times 100$  magnification) of the HCC44, HCC2429, H1568, H1703, H1563, H1568, and HCC1359 cells 2 weeks after transduction with viruses encoding either control or DNA-PKcs targeting shRNA. **D**, induction of apoptosis by 1 μmol/L treatment with KU60648 (0, 24, 48, 72, and 96 hours) in *Msh3*<sup>-/-</sup> (blue) and *Msh3*<sup>wt/wt</sup> control (gray) murine embryonic fibroblasts as assessed by flow cytometry (annexin-V/PI double-positive populations). Error bars, SD of three independent experiments.

carry a *BRD4*–NUT fusion, were included as positive controls. Upon completion of drug exposure, cells were stained with propidium iodide (PI), and relative cellular DNA content was assessed by flow cytometry. As shown in Supplementary Fig. S4, all nine cell lines displayed an early prominent loss of the S-phase populations (6 and 12 hours), followed by a subsequent decrease of cells with 4N DNA content (24 hours). Intriguingly, KU60648-resistant cell lines showed a remarkable reconstitution to the initial cell-cycle profiles of untreated cells (Supplementary Fig. S4), strongly suggesting full cell-cycle checkpoint recovery and restart of proliferation. In marked contrast, all KU60648-sensitive cells had a persistent loss of S- and G<sub>2</sub>–M populations (Supplementary Fig. S4), rationalizing the results of our CellTiter-Glo-based screen (Fig. 1A and Supplementary Fig. S1C). To validate these

distinct cellular response patterns, we next used immunoblotting (Fig. 2A). Exposure of the *MSH3*-mutant cell lines HCC44, H1838, and HCT116, as well as the positive control HCC2429 to 1 μmol/L KU60648 (48 hours), resulted in a substantial loss of S-phase cyclin A2 expression, corroborating the persistent cell-cycle arrest observed in our flow cytometry experiments (Fig. 2A, top). In contrast, the *MSH3*-proficient control lines H2347, H1568, HCC1359, and H1915 displayed continued cyclin A2 expression after 48-hour treatment with 1 μmol/L of KU60648 (Fig. 2A, bottom).

We next asked whether the KU60648-sensitive cell lines also displayed signs of apoptotic cell death. Therefore, we used immunoblotting to detect cleaved caspase-3, as a marker for apoptosis. Consistent with the results of our initial screen, the sensitive cell lines HCC44, H1838, and HCT116 and the

positive control HCC2429 displayed cleavage of caspase-3 after KU60648 treatment (1 μmol/L, 48 hours), indicating execution of apoptosis (Fig. 2A, top). In marked contrast, no caspase-3 cleavage could be observed after KU60648 treatment (1 μmol/L, 48 hours) in the *MSH3*-proficient control lines H2347, H1568, HCC1359, and H1915 (Fig. 2A, bottom).

To further validate KU60648-induced apoptosis with an independent assay, we used flow cytometry (Fig. 2B) and stained cells with annexin-V and PI after 72 hours of KU60648 exposure (0, 0.1, 0.5, and 1 μmol/L). We note that the resistant cells had shown full recovery of proliferation after 72 hours of sustained KU60648 treatment (Supplementary Fig. S4). As indicated by the appearance of a large annexin-V/PI double-positive population in the *MSH3*-mutant cells following KU60648 exposure, the reduced viability that we observed in the initial screen was likely attributable to massive apoptosis (Fig. 2B). Similar effects were observed in the positive control lines (HCC2429, *BRD4-NUT*, and H1563, *BRCA1*-mutant). In contrast, even 1 μmol/L of KU60648 did not result in any substantial apoptosis in *MSH3*-proficient control cells ( $P = 0.011$ ; Fig. 2B).

As KU60648 treatment has been reported to induce DSBs, we next asked whether the DSB-inducing anthracycline drug doxorubicin might synergistically enhance KU60648 activity in *MSH3*-mutant cells. For this purpose, we examined the effect of 120 different concentration combinations of KU60648 and doxorubicin on three *MSH3*-mutant (HCT116, HCC44, and H1838) and three control lines (H1915, H1568, and HCC1359; Supplementary Fig. S5A). We used CellTiter-Glo assays as readout for cellular viability after 48 and 96 hours of compound exposure. For each concentration, we compared the observed residual viability with the expected viability, assuming additive effects of both compounds (Bliss independence; Supplementary Fig. S5A). We found that doxorubicin was active on most cells examined, without discriminating between *MSH3*-deficient and -proficient lines. However, the effect of doxorubicin (50–250 nmol/L) was synergistically enhanced by cotreatment with KU60648 (~1 μmol/L) for *MSH3*-deficient cell lines only; additive effects of both compounds were observed for the *MSH3*-proficient controls (Supplementary Fig. S5A).

We next compared apoptosis levels under cotreatment with KU60648 (1 μmol/L) and doxorubicin (0, 30, 100, 250, and 1,000 nmol/L) with induction of apoptosis under single-agent therapy. Again, we detected synergistic induction of apoptosis exquisitely for *MSH3*-deficient cell lines at low and variable concentrations of doxorubicin (Supplementary Fig. S5B).

In summary, our experiments underscore the functional relevance of the observations made in our high-throughput cell line-based screen. These data strongly suggest that DNA-PKcs inhibition results in the apoptotic demise of *MSH3*-mutant cells (Fig. 2A and B and Supplementary Fig. S4). The cytotoxic effect of KU60648 on *MSH3*-mutant cells can be further increased by combination with low concentrations of doxorubicin. However, this combination is less discriminative between *MSH3*-deficient and -proficient cells (Supplementary Fig. S6).

### Genetic Validation of the Apparent Synthetic Lethality between *MSH3* and *PRKDC*

As studies with ATP-competitive inhibitors are frequently hampered by off-target effects, we next performed genetic experiments to functionally confirm DNA-PKcs (encoded

by *PRKDC*) as the target of KU60648 in *MSH3*-mutant and *BRCA1*-defective cell lines (Fig. 2C and D and Supplementary Figs. S6–S8). We used RNA interference (RNAi) to deplete DNA-PKcs in four sensitive and two resistant control lines (Fig. 2C). Knockdown efficiency was confirmed by immunoblotting (Supplementary Fig. S6). Confirming that repression of DNA-PKcs expression leads to the induction of apoptosis in *MSH3*-mutant settings, we reproducibly detected cleavage of caspase-3 in KU60648-sensitive cell lines (HCC44 and HCC2429), 120 hours following viral short hairpin RNA (shRNA) delivery (Supplementary Fig. S6). Next, we assessed the effects of RNAi-mediated repression of *PRKDC* in colony formation assays (Fig. 2C). Two weeks after viral RNAi delivery, we observed complete eradication of KU60648-sensitive HCC44, H1703, HCC2429, and H1563 lines, whereas KU60648-resistant H1568 and HCC1359 lines did not exhibit any signs of morphologic change (Fig. 2C).

We next examined whether other components of the NHEJ pathway might be similarly synthetically lethal with *MSH3*. DNA damage repair by NHEJ is initiated by a complex formed by the proteins KU70 (encoded by *XRCC6*) and KU80 (encoded by *XRCC5*). Hence, we compiled five shRNA constructs specifically targeting KU80 and transduced four independent cell lines (HCT116 [*MSH3*<sup>mut</sup>], HCC44 [*MSH3*<sup>mut</sup>], HCC1359 [cntrl], and H1568 [cntrl]) with each of these constructs. We assessed knockdown efficiency by immunoblotting (Supplementary Fig. S7A) to choose two shRNAs (shXRCC5 #1 and shXRCC5 #3) that effectively silenced expression of KU80.

In colony formation assays, we observed mild growth-arrestive effects of KU80 depletion in the *MSH3*-proficient cell lines, indicating that KU80 is critical for cell survival in general (Supplementary Fig. S7B and S7C). In contrast, strong cytotoxic effects were detected in *MSH3*-deficient cells for both constructs targeting KU80 (Supplementary Fig. S7B and S7C). Therefore, shRNA-mediated suppression of an independent NHEJ protein had similar cytotoxic effects in *MSH3*-deficient cells as knockdown of *PRKDC*.

Next, we compared the KU60648 response of *Msh3*-proficient and *Msh3*-deficient murine embryonic fibroblasts (MEF) to validate *Msh3* deficiency as a genetic determinant of DNA-PKcs addiction (Supplementary Fig. S8A). In brief, we first assessed KU60648 potency in *Msh3<sup>wt/wt</sup>* and *Msh3<sup>-/-</sup>* MEFs using CellTiter-Glo assays under the same conditions as in our initial screen. As shown in Supplementary Fig. S8B, *Msh3*-deficient MEFs were significantly more sensitive to DNA-PKcs inhibition than their isogenic *Msh3*-proficient counterparts ( $P = 9.33 \times 10^{-5}$ ). To further characterize the nature of this response, we assessed KU60648-induced apoptosis by immunoblotting and flow cytometry (Fig. 2D and Supplementary Fig. S8C). We observed caspase-3 cleavage (Supplementary Fig. S8C) and the appearance of an annexin-V/PI double-positive population (Fig. 2D) in *Msh3*-deficient MEFs, strongly suggesting that DNA-PKcs inhibition results in apoptosis in *Msh3*-defective settings. In stark contrast, neither caspase-3 cleavage nor appearance of an annexin-V/PI double-positive apoptotic population could be detected in *Msh3*-proficient MEFs (Fig. 2D and Supplementary Fig. S8C). Together, genetic repression of *PRKDC* in *MSH3*-mutant cells, on the one hand (Fig. 2C and Supplementary Fig. S6), and pharmacologic inhibition of DNA-PKcs activity in

*Msh3*-deficient cells, on the other hand (Fig. 2D and Supplementary Fig. S8), cross-validated the proposed synthetic lethal interaction between these two genes. Furthermore, the cytotoxic effects, which we observed in *MSH3*-mutant cells under suppression of KU80 expression (Supplementary Fig. S7), might suggest a generalizable synthetic lethal interaction between the homologous recombination and NHEJ pathways.

### MSH3-Defective Cell Lines Display a Defect in Homologous Recombination-Based DSB Repair

Our initial screen revealed that alterations in homologous recombination-mediated DSB repair are associated with DNA-PKcs inhibitor sensitivity (Fig. 1 and Supplementary Figs. S1 and S2). Thus, we next asked whether homologous recombination defects were responsible for the DNA-PKcs addiction that we observed in *MSH3*-mutant cells. To this end, we transiently incubated *MSH3*-proficient (H1568, HCC1359, and *Msh3*<sup>w/w</sup> MEFs) and *MSH3*-defective (HCC44, H1838, HCT116, RL95-2, H1703, and *Msh3*<sup>-/-</sup> MEFs) cells with the DSB-inducing topoisomerase II inhibitor etoposide (0.1 μmol/L, 1-hour pulse) to induce tractable DSBs. As *BRCA1* loss-of-function had previously been shown to result in severely impaired homologous recombination-mediated DSB repair (7, 11), we also studied the *BRCA1*-mutant H1563 cell line (Fig. 3 and Supplementary Fig. S9A).

To examine the DSB repair kinetics in our cell line panel, we used indirect immunofluorescence to monitor the persistence of etoposide-induced γ-H2AX nuclear foci as an established marker for unrepaired DSBs (1). We observed robust formation of γ-H2AX nuclear foci in all cell lines that were analyzed 4 hours following removal of etoposide (Fig. 3A and B and Supplementary Fig. S9A), whereas no nuclear γ-H2AX foci could be detected in untreated cells. However, 72 hours after etoposide removal, these foci had disappeared in all cell lines (Fig. 3A and B and Supplementary Fig. S9A), suggesting that both *MSH3*-proficient and *MSH3*-defective, as well as *BRCA1*-mutant, cells were capable of repairing etoposide-induced DSBs.

In a parallel set of experiments, we stained these cells with an antibody detecting RAD51 nuclear foci (Fig. 3A and C and Supplementary Fig. S9A), which are a hallmark feature of ongoing homologous recombination-mediated DSB repair (11). Of note, *BRCA1*-deficient cells were previously shown to lack RAD51 foci formation in response to DSB-inducing agents (7, 11). As shown in Fig. 3 and Supplementary Fig. S9A, the *MSH3*- and *BRCA1*-proficient H1568 and HCC1359, as well as wild-type MEFs, displayed prominent nuclear RAD51 foci 4 hours after the removal of etoposide, suggesting functional homologous recombination-mediated DSB repair. Nuclear RAD51 foci were not detectable in these cell lines 72 hours after etoposide removal, suggesting complete DSB repair. In marked contrast, RAD51 foci could not be detected within a 72-hour time frame after etoposide removal in either the *MSH3*-defective (HCC44, H1838, HCT116, RL95-2, H1703, and *Msh3*<sup>-/-</sup> MEFs) or the *BRCA1*-mutant H1563 cells ( $P = 2.3 \times 10^{-3}$ ; Fig. 3A and C and Supplementary Fig. S9A). These data strongly suggest that the homologous recombination-mediated repair of etoposide-induced DSBs is substantially impaired in *MSH3*-mutant cells. Similar effects have been previously described for *BRCA1* deficiency (Fig. 3A and C; ref. 11).

### Homologous Recombination Deficiency Rationalizes the Synthetic Lethality between *MSH3* and PRKDC

Given the substantial homologous recombination defect that we had observed in *MSH3*-mutant cells (Fig. 3 and Supplementary Fig. S9A), we next hypothesized that pharmacologic NHEJ abrogation through DNA-PKcs inhibition might lead to the generation of persistent unrepaired DSBs in these cells. To directly test this hypothesis, we induced DSBs in homologous recombination-proficient (H1568, HCC1359, and *Msh3*<sup>w/w</sup> MEFs) and homologous recombination-defective (HCC44 [*MSH3*<sup>mut</sup>], H1838 [*MSH3*<sup>mut</sup>], HCT116 [*MSH3*<sup>mut</sup>], RL95-2 [*MSH3*<sup>mut</sup>], H1703 [*MSH3*<sup>mut</sup>], *Msh3*<sup>-/-</sup> MEFs, and H1563 [*BRCA1*<sup>mut</sup>]) cells by applying an etoposide pulse (0.1 μmol/L, 1 hour) in the absence or continued presence of 0.5 μmol/L of KU60648. Cells were protected from premature apoptosis by the addition of the irreversible pan-caspase inhibitor Z-VAD (10 μmol/L), which was applied together with etoposide. Similar to the experiments detailed in Fig. 3, we performed immunofluorescence to detect nuclear γ-H2AX and RAD51 foci (Fig. 4 and Supplementary Fig. S9B). Recruitment of RAD51, the core component of the homologous recombination machinery, to DSBs requires prior resection of DNA ends to generate RPA-coated 3' ssDNA overhangs (28). To monitor the occurrence of 3' ssDNA repair intermediates in our cell line panel, we thus also included a set of experiments in which we monitored nuclear RPA1 foci as a marker for ssDNA. As shown in Fig. 4A-C and Supplementary Fig. S9B, 4 hours after etoposide removal, prominent γ-H2AX foci could be detected in all cell lines, in both the absence or presence of KU60648. No γ-H2AX foci could be detected in the absence of KU60648 72 hours following etoposide removal. Similarly, we observed no γ-H2AX foci in the homologous recombination-proficient cells 72 hours after etoposide pulse treatment, even when KU60648 was present. In stark contrast and consistent with a severe DSB repair defect, γ-H2AX foci could be visualized 72 hours following etoposide removal in the homologous recombination-defective cells that were continuously exposed to KU60648. Intriguingly, the staining patterns for RPA1 foci were identical to those observed for γ-H2AX foci (Fig. 4A, D, and E and Supplementary Fig. S9B). The persistent presence of RPA1 foci in homologous recombination-defective cells that were treated with KU60648 strongly suggests that DSBs are resected in these cells. However, the continued presence of γ-H2AX foci indicates that DSBs cannot be repaired in homologous recombination-defective cells when NHEJ is pharmacologically abrogated. In summary, our immunofluorescence data lend strong support to the hypothesis that *MSH3* mutations result in a homologous recombination defect. Impaired homologous recombination proficiency renders *MSH3*-mutant cells dependent on functional DNA-PKcs-mediated NHEJ to repair DSBs.

### In Vivo Validation of DNA-PKcs as an Actionable Target in *MSH3*-Defective Tumors

Human tumors frequently display an activated DDR, likely as a result of stalled replication forks and DSBs (29–31). These genotoxic lesions are thought to be the molecular equivalent of oncogene-induced replicative stress and unscheduled replication firing (29, 32). This presence of genotoxic stress in otherwise untreated human neoplastic lesions led us to

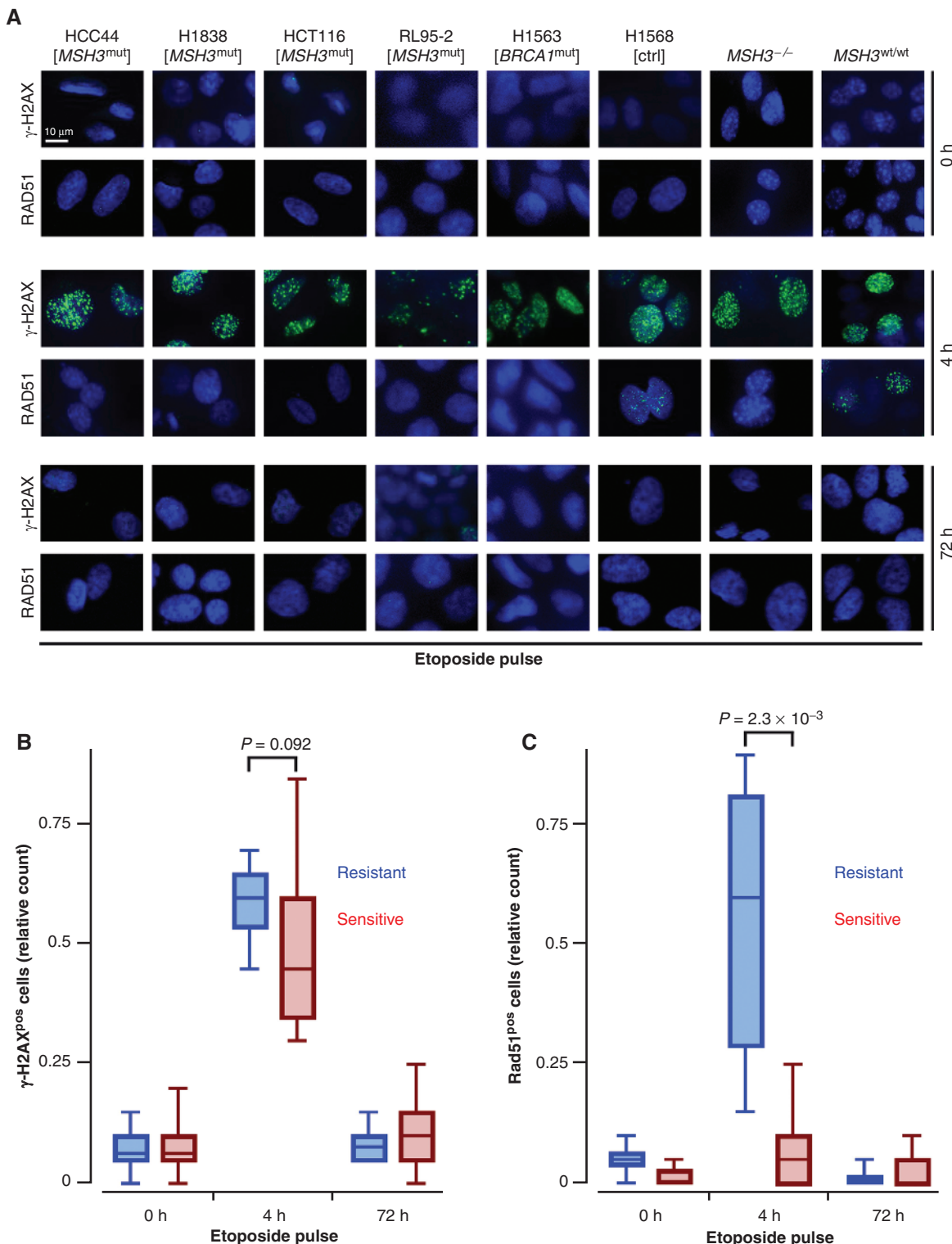
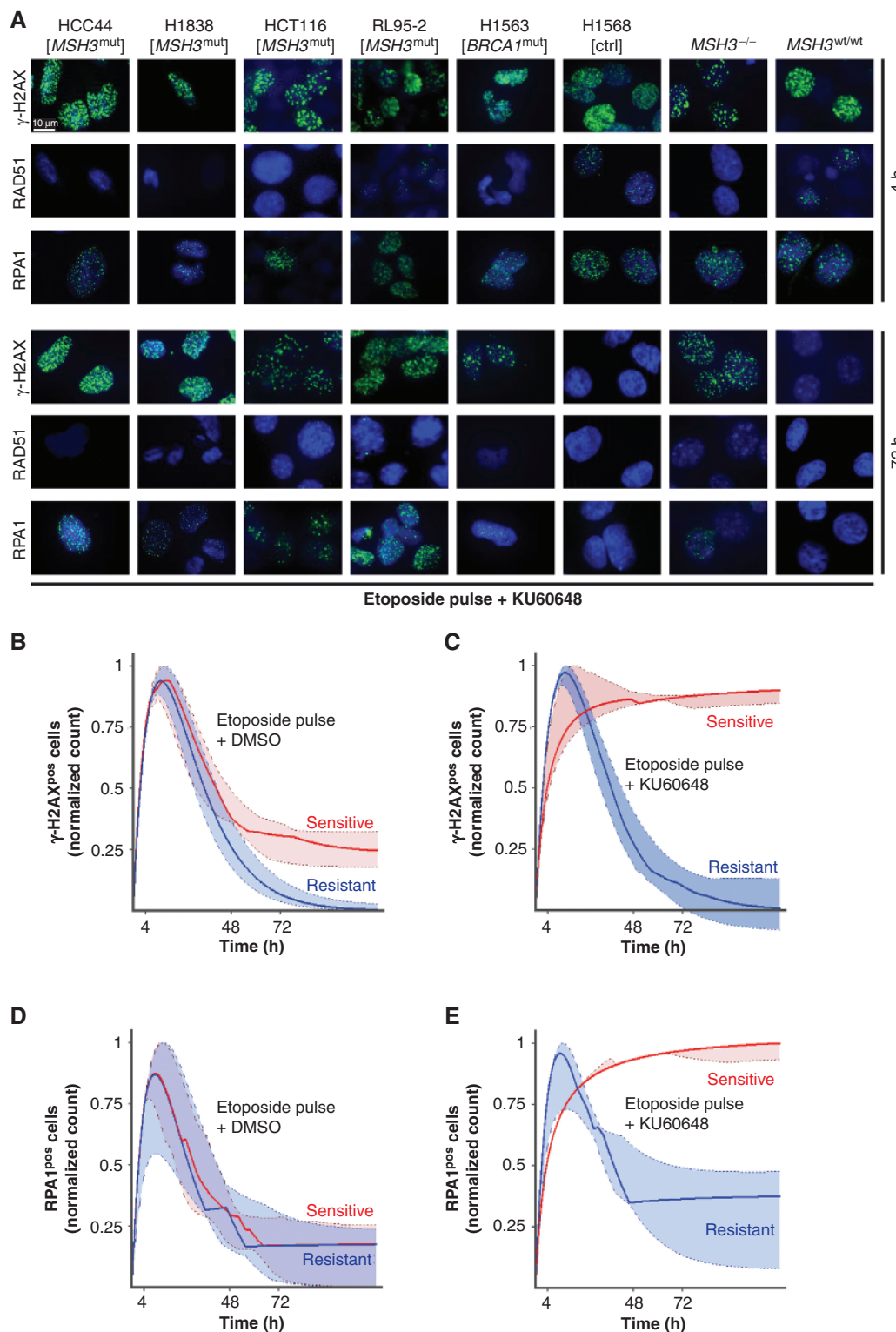


**Figure 3.** MSH3-mutant or MSH3-deficient cells display a robust homologous recombination defect. **A**, DNA DSB repair kinetics were monitored (0, 4, and 72 hours) after short (1 hour) exposure to a low-dose (0.1  $\mu$ mol/L) etoposide pulse. Representative immunofluorescence images [green,  $\gamma$ -H2AX or RAD51 nuclear foci; blue, 4',6-diamidino-2-phenylindole (DAPI) counterstain] are shown for HCC44 [MSH3<sup>mut</sup>], H1838 [MSH3<sup>mut</sup>], HCT116 [MSH3<sup>mut</sup>], RL952 [MSH3<sup>mut</sup>], H1563 [BRCA1<sup>mut</sup>], and H1568 [ctrl] cancer cell lines, as well as Msh3<sup>-/-</sup> and Msh3<sup>wt/wt</sup> MEFs. **B**, box plot diagrams display the quantification of  $\gamma$ -H2AX stains for the experiment shown in **A** in 9 independent cancer cell lines. Significance values were derived from comparing  $\gamma$ -H2AXfoci-positive cell counts (4 hours) by t test;  $n = 3$ . **C**, box plot diagrams representing the quantification of RAD51 foci for the experiment shown in **A** in nine independent cancer cell lines. Significance levels were determined by t test;  $n = 3$ .

Downloaded from http://cancerdiscovery.aacrjournals.org/cancerdiscovery/article-pdf/4/5/592/1845029/552.pdf by guest on 14 August 2024



Downloaded from http://cancerdiscovery.aacrjournals.org/cancerdiscovery/article-pdf/4/5/592/1845029/552.pdf by guest on 14 August 2024

**Figure 4.** Homologous recombination-defective *MSH3*-mutant cells fail to repair DNA DSBs when DNA-PKcs is pharmacologically repressed. **A**, DNA DSB repair kinetics were monitored (4 and 72 hours) after short (1 hour) exposure to low-dose (0.1  $\mu$ mol/L) pulses of etoposide and permanent DNA-PKcs inhibition (1  $\mu$ mol/L KU60648). Representative immunofluorescence images [green,  $\gamma$ -H2AX, RAD51, or RPA1 foci; blue, 4',6-diamidino-2-phenylindole (DAPI) counterstain] are shown for HCC44 [*MSH3*<sup>mut</sup>], H1838 [*MSH3*<sup>mut</sup>], HCT116 [*MSH3*<sup>mut</sup>], RL952 [*MSH3*<sup>mut</sup>], H1563 [*BRCA1*<sup>mut</sup>], and H1568 [ctrl] cancer cell lines, as well as *Msh3*<sup>-/-</sup> and *Msh3*<sup>wt/wt</sup> MEFs. **B–E**,  $\gamma$ -H2AX (**B** and **C**) and RPA1 (**D** and **E**) stains (0, 4, 48, and 72 hours) of the experiment shown in **A** were quantified (normalized to the maximum of each cell line) and interpolated by a generalized Hubbert function. Medians (y-axis) of interpolation curves ( $n = 9$  independent cell lines;  $n = 3$  biologic replicates) are plotted against time after etoposide exposure (x-axis) for KU60648-sensitive (red) and KU60648-resistant (blue) cell lines. Quartiles are shown as envelopes (dashed lines).

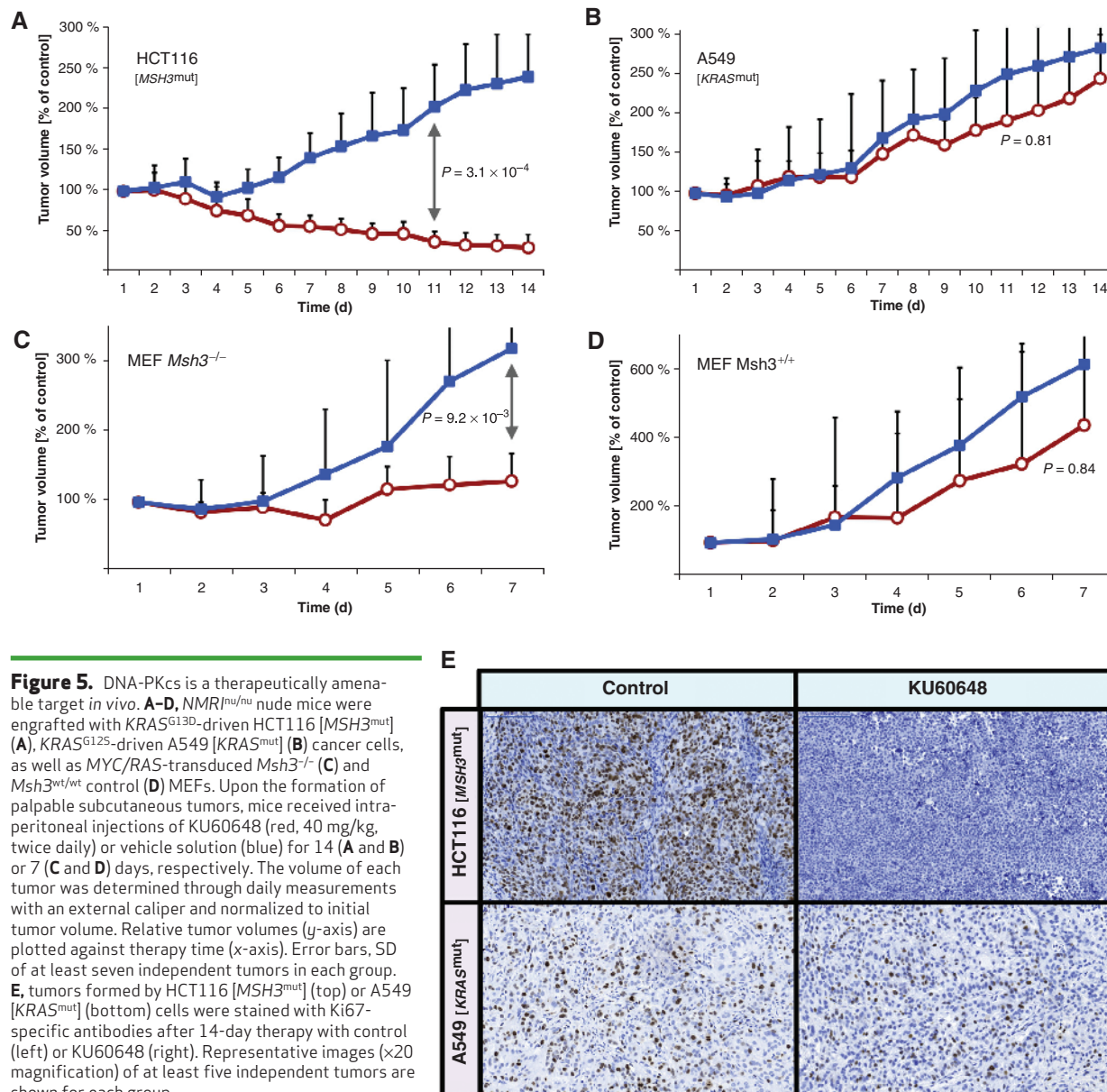


**Figure 5.** DNA-PKcs is a therapeutically amenable target *in vivo*. **A–D**, NMR<sup>nu/nu</sup> nude mice were engrafted with KRAS<sup>G13D</sup>-driven HCT116 [MSH3<sup>mut</sup>] (**A**), KRAS<sup>G12S</sup>-driven A549 [KRAS<sup>mut</sup>] (**B**) cancer cells, as well as MYC/RAS-transduced Msh3<sup>-/-</sup> (**C**) and Msh3<sup>wt/wt</sup> control (**D**) MEFs. Upon the formation of palpable subcutaneous tumors, mice received intraperitoneal injections of KU60648 (red, 40 mg/kg, twice daily) or vehicle solution (blue) for 14 (**A** and **B**) or 7 (**C** and **D**) days, respectively. The volume of each tumor was determined through daily measurements with an external caliper and normalized to initial tumor volume. Relative tumor volumes (y-axis) are plotted against therapy time (x-axis). Error bars, SD of at least seven independent tumors in each group. **E**, tumors formed by HCT116 [MSH3<sup>mut</sup>] (top) or A549 [KRAS<sup>mut</sup>] (bottom) cells were stained with Ki67-specific antibodies after 14-day therapy with control (left) or KU60648 (right). Representative images ( $\times 20$  magnification) of at least five independent tumors are shown for each group.

investigate whether endogenous DNA damage, specifically in homologous recombination-defective tumors, might offer a therapeutic window for the use of DNA-PKcs inhibitors *in vivo*. The strong and robust effects that we observed in homologous recombination-defective MSH3-mutant cells under DNA-PKcs inhibition *in vitro* (Figs. 1 and 2) motivated us to further assess its efficiency as a single agent *in vivo*. To this end, we used an NMR<sup>nu/nu</sup> xenograft mouse model to study therapeutic drug response *in vivo*. In brief, we subcutaneously engrafted nude mice either with KRAS-driven, MSH3-mutant HCT116 cells, or with MYC/HRAS<sup>G12V</sup> double-transduced Msh3-deficient MEFs (Fig. 5A–E and Supplementary Fig. S10A–S10F). For negative controls, we used either KRAS-mutant A549 cells or MYC/HRAS<sup>G12V</sup> double-transduced Msh3-proficient MEFs (Fig. 5A–E and Supplementary Fig. S10A–S10F).

As described previously (14), we administered 40 mg/kg doses of the DNA-PKcs inhibitor KU60648 twice daily (intra-

peritoneal injection). Intriguingly, we observed a substantial (final tumor volume, 31.5%) and significant ( $P = 3.1 \times 10^{-4}$ ; Fig. 5A and Supplementary Fig. S10A and S10E) tumor volume shrinkage for HCT116-driven tumors under KU60648 therapy within 14 days, whereas A549 control tumors were completely resistant and even showed continued volume gains under KU60648 therapy (Fig. 5B and Supplementary Fig. S10B and S10F). To further compare the tumor proliferation rate between both therapy groups, we stained tumor samples with Ki67-specific antibodies after 14-day therapy (Fig. 5E). Shrinkage of HCT116 tumors translated into complete eradication of the Ki67-positive cell fraction under KU60648 therapy. In marked contrast, the Ki67 staining of A549 tumors remained stable between control and therapy groups, indicating their maintained proliferation under therapy (Fig. 5E).

Tumors driven by MYC/HRAS<sup>G12V</sup> double-transduced MEFs displayed a more aggressive phenotype than the HCT116/

A549–driven tumors (Fig. 5C and D and Supplementary Fig. S10C and S10D). Thus, tumor volumes could be followed for only 7 days before control animals had to be sacrificed. Despite this highly aggressive growth behavior, therapy with KU60648 resulted in stable disease (final tumor volume, 109%) of *Msh3*<sup>-/-</sup> MEF-driven lesions, whereas we did not observe any significant therapeutic effect of KU60648 on *Msh3*<sup>wt/wt</sup> MEF-driven tumors (Fig. 5C and D and Supplementary Fig. S10C and S10D). In summary, our results strongly recommend DNA-PKcs as a promising drug target for the rational design of personalized therapies for homologous recombination–defective neoplastic disease. Specifically, the therapeutic effect on *Msh3*-knockout MEFs and tumors derived from these cells confirms that loss-of-function mutations in *MSH3* are genetic and functional predictors of DNA-PKcs inhibitor activity *in vivo*.

## DISCUSSION

### Alterations in Homologous Recombination Signaling Are Associated with DNA-PKcs Addiction

Eukaryotic cells have evolved a plethora of DNA repair pathways, which together function to maintain genomic integrity of multicellular organisms (2). Perhaps not surprisingly, inactivating mutations in these DNA repair pathways are commonly observed in human tumors and are thought to fuel a “mutator phenotype” (33–35). For instance, cancer genome resequencing data suggest that approximately 50% of high-grade serous ovarian carcinomas are homologous recombination defective (36).

We have previously reported an actionable synthetic lethal interaction between the homologous recombination gene *ATM* and the critical NHEJ gene *PRKDC* (13, 14, 37). In addition, the combined knockout of *ATM* and *PRKDC* was recently shown to result in embryonic lethality at E7.5 in mice (12). Intriguingly, E7.5 is a developmental stage at which embryonic cells are hypersensitive to DNA damage (12). On the basis of these observations, we hypothesized that mutations in additional homologous recombination genes might be associated with a similar DNA-PKcs addiction.

To systematically decipher additional genetic aberrations that are associated with DNA-PKcs addiction, we first linked large-scale sequencing data (16) to high-throughput KU60648 activity profiling across 67 cancer cell lines (Fig. 1). As reported recently (38), potency and selectivity of several compounds are underestimated, if analysis is restricted to their half maximal growth-inhibitory concentrations ( $GI_{50}$ ). Hence, we amended our interpretation of the cell line screen by Hill coefficients and nearest-neighbor distances (Supplementary Fig. S1). Using this approach, we found that mutations in genes involved in DNA repair ( $P = 2.98 \times 10^{-12}$ ) significantly associated with KU60648 sensitivity. More precisely, we were able to confirm mutations in several genes with a known role in homologous recombination–mediated DSB repair, including *BRCA1*, *BRCA2*, *ATM*, *CHEK2*, *RAD50*, *SMC2*, and *PAXIP*, to predict DNA-PKcs addiction (Fig. 1 and Supplementary Fig. S2). Intriguingly, the therapeutic response of homologous recombination–defective cancer cells to KU60648 seemed to be independent of *TP53* mutation status (Fig. 1A). This observation strongly suggests that DNA-PKcs inhibition in homologous recombination–defective tumors might be a viable therapeutic strategy to selectively target *TP53*-defective lesions, which are typically

resistant against most first-line anticancer agents, such as chemotherapy and radiotherapy.

To our surprise, we identified *MSH3* as a strong determinant for KU60648 sensitivity, which we showed to be involved in homologous recombination–mediated DSB repair in follow-up experiments (Figs. 1–4). There is accumulating circumstantial evidence suggesting a role for the *MSH2*–*MSH3* complex in DSB repair (39–43). For instance, RNAi-mediated *MSH3* depletion has recently been shown to result in substantially delayed *RAD51* loading after 2-Gy ionizing radiation (25). Here, we demonstrate that *MSH3* mutation or deficiency is associated with a homologous recombination defect due to impaired *RAD51* loading (Fig. 3). More importantly, we link this *MSH3* deficiency–associated homologous recombination defect to a druggable DNA-PKcs addiction *in vitro* (Fig. 2) and *in vivo* (Fig. 5).

### Therapeutically Targeting the Synthetic Lethal Interaction between *MSH3* and *PRKDC*

We genetically validated the synthetic lethal interaction between *MSH3* and *PRKDC* that emerged from our initial screen (Fig. 2). To this end, we showed that pharmacologic DNA-PKcs inhibition in *Msh3* knockout MEFs resulted in the induction of massive apoptosis, compared with *Msh3*-proficient isogenic control cells. Conversely, RNAi-mediated repression of *PRKDC* resulted in apoptotic demise of *MSH3*-mutant cancer cells, whereas *MSH3*-proficient control cells were largely unaffected by *PRKDC* knockdown (Figs. 2 and 6).

Functionally, we demonstrate that *MSH3* knockout results in substantially impaired homologous recombination–mediated DSB repair due to delayed *RAD51* loading (Fig. 3). However, *MSH3* deficiency did not completely abrogate etoposide-induced DSB repair. In fact, *MSH3*-defective cells remained capable of repairing etoposide-induced genotoxic lesions, likely through recruitment of alternative DSB repair pathways, such as NHEJ (Figs. 3 and 6). However, pharmacologic inhibition of the essential NHEJ kinase DNA-PKcs completely prevented etoposide-induced DSB repair and led to the generation of ssDNA repair intermediates, which have previously been shown to represent a chromatin structure that triggers apoptosis (6, 14, 44). Moreover, we observed early loss of S-phase for all cell lines under KU60648 treatment (Supplementary Fig. S4). However, only KU60648-resistant cells were able to repair KU60648-induced DNA damage and returned to normal cell-cycle profiles within 48 hours. Together, these observations mechanistically rationalized the massive induction of apoptosis that we detected by immunoblotting and flow cytometry (Fig. 2).

### Clinical Perspective

Our data reported here strongly suggest that the synthetic lethal interaction between the NHEJ kinase DNA-PKcs and multiple homologous recombination genes, including *BRCA1*, *BRCA2*, *ATM*, *CHEK2*, *RAD50*, *SMC2* and *PAXIP*, might be therapeutically exploited in patients with homologous recombination–defective neoplastic disease. Thus, it might be desirable to include genetically stratified patient cohorts into next-generation clinical trials with DNA-PKcs inhibitors, such as CC-115, a dual mTOR/DNA-PKcs inhibitor, currently being evaluated in phase I trials (45).

A recent study conducted a genome-scale analysis of 276 colorectal tumors and identified somatic *MSH3* loss-of-function

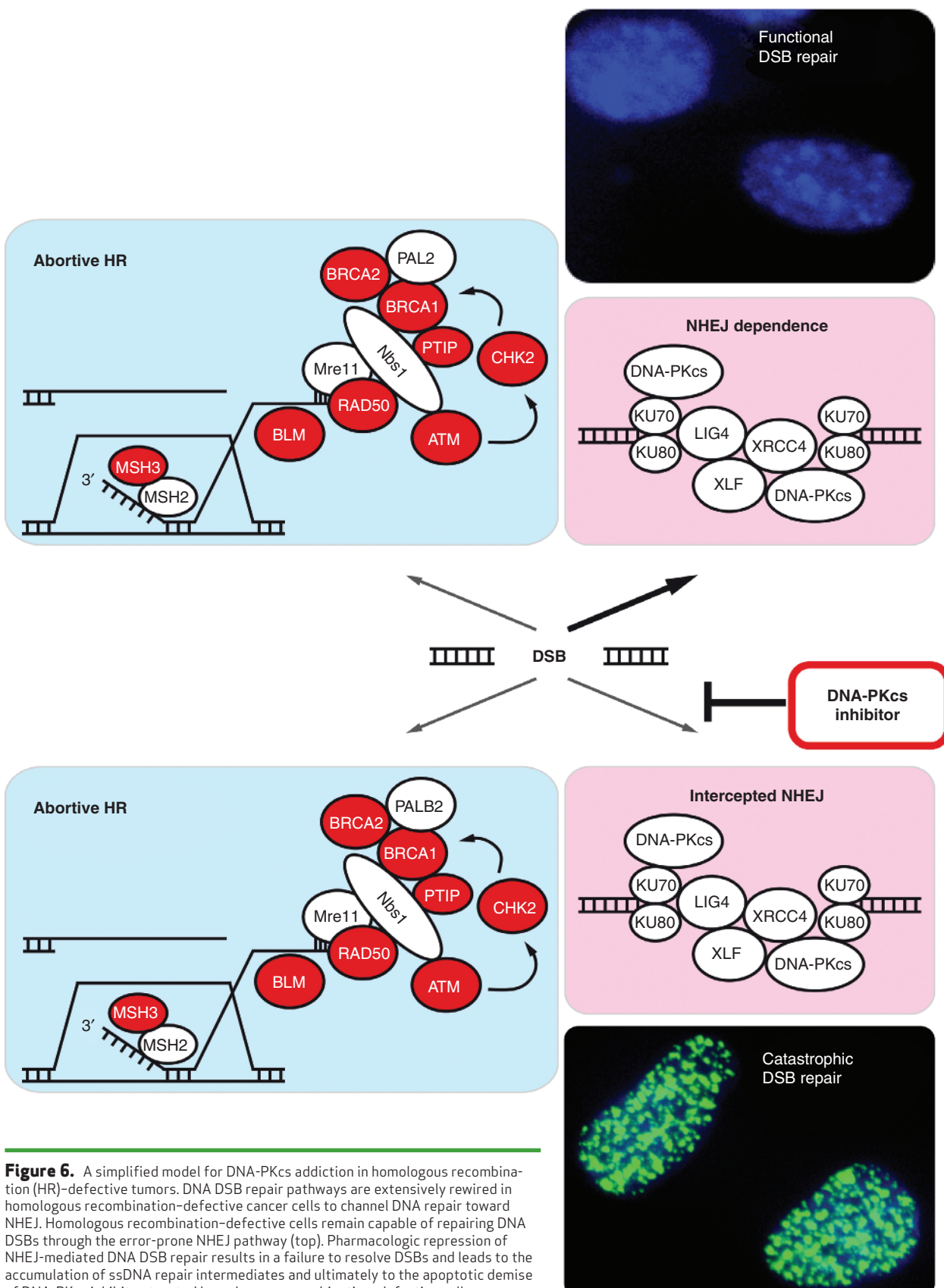


**Figure 6.** A simplified model for DNA-PKcs addiction in homologous recombination (HR)-defective tumors. DNA DSB repair pathways are extensively rewired in homologous recombination-defective cancer cells to channel DNA repair toward NHEJ. Homologous recombination-defective cells remain capable of repairing DNA DSBs through the error-prone NHEJ pathway (top). Pharmacologic repression of NHEJ-mediated DNA DSB repair results in a failure to resolve DSBs and leads to the accumulation of ssDNA repair intermediates and ultimately to the apoptotic demise of DNA-PKcs inhibitor-treated homologous recombination-defective cells.

mutations in approximately 7% of all samples and 40% of all hypermutated, MSI tumors (46). Thus, disabling *MSH3* mutations are present in a substantial fraction of colorectal cancer, which represents one of the most common cancer entities in the Western world. To the best of our knowledge, this is the first study that discovers a molecular liability in *MSH3*-mutant neoplastic disease that is amenable for pharmacologic intervention both *in vitro* and *in vivo*. Thus, our findings might have direct therapeutic impact on the clinical care of patients suffering from *MSH3*-mutant MSI colorectal cancer. Furthermore, biopsies retrieved from MSI colorectal cancers should be both sequenced to determine *MSH3* status and stained for RAD51 foci, after short exposure to high-dose etoposide, to identify those patients who are most likely to benefit from a DNA-PKcs inhibitor therapy.

## METHODS

### Cell Lines and Reagents

All human cell lines were obtained from the American Type Culture Collection ([www.atcc.org](http://www.atcc.org)) and cultured in RPMI or Dulbecco's Modified Eagle Medium (DMEM), supplemented with 10% of fetal calf serum (FCS) at 37°C in a humidified incubator supplied with 5% CO<sub>2</sub>. Cell lines were authenticated by genotyping (SNP 6.0 arrays; Affymetrix), and all cell lines were tested for infection with *Mycoplasma* (MycoAlert; Lonza).

Compounds were purchased from Axon Medchem (KU60648) or Sigma-Aldrich (etoposide and doxorubicin), dissolved in water or dimethyl sulfoxide (DMSO), and stored as aliquots at -80°C or -20°C. Two independent lots were tested for each compound.

Retroviral packaging constructs pMDg and pMDg/p were a kind gift from T. Benzing (University Hospital, Cologne, Germany). Plasmids containing shRNA targeting *PRKDC* (V2HS 233593) were obtained from J.B. Lazoro (Dana-Farber Cancer Institute, Boston, MA), and retroviral plasmids for double transduction of MEFs (pBabe-MYC and pBabe-HRAS<sup>G12V</sup>) were kindly provided by T. Brummelkamp (NKI-AVL, Amsterdam, the Netherlands). Plasmids containing shRNA targeting KU80 (TRCN10468, TRCN18363, TRCN288701, TRCN295856, and TRCN307986) were purchased from Sigma-Aldrich. Viral gene delivery was performed as described previously (50).

### Cell Line-Based Screening

High-throughput cell line-based screening was performed as described previously (47). In brief, cell lines were plated in triplicate into sterile 96-well plates at 1,000 cells per well density and treated with 10 increasing concentrations (range, 1 nmol/L–2 μmol/L) of KU60648 for 96 hours. Relative cell viability was determined by measuring the ATP content (CellTiter-Glo; Promega) and normalizing it to the untreated control. Measurements were repeated if half-maximal inhibitory concentrations (GI<sub>50</sub>) of triplicates differed by more than 10% or if the average GI<sub>50</sub> value was lower than 400 nmol/L.

### Genetic Compound Activity Prediction

For the calculation of GI<sub>50</sub>, concentration-viability curves were interpolated by logistic functions (R package "ic50"; ref. 48). For each concentration (range, 150 nmol/L–1 μmol/L), we calculated the distance to its nearest neighbor in the KU60648 screening activity profile to infer a suitable GI<sub>50</sub> threshold. We used this threshold to classify cells into KU60648-sensitive and KU60648-resistant lines.

We next annotated all cell lines for which sequencing data were available in the Cancer Cell Line Encyclopedia database (MAF files; ref. 16) by their protein-coding mutations. We tested for each gene whether mutations were more frequent in the KU60648-sensitive cohort than in the group of resistant cell lines by the Fisher exact test. In addition,

we calculated for each gene its sensitivity effect by comparing GI<sub>50</sub> values between mutant versus wild-type cell lines. For missense mutations, we predicted their functional effect on global protein structure by the PolyPhen-2 algorithm (49).

### Xenograft Mouse Models

All animal procedures were approved by the local animal protection committee and the local authorities. Six- to 10-week-old male *NMRI*<sup>nu/nu</sup> mice (CRL:NMRI-FOXN1 NU; Charles River Laboratories) were subcutaneously engrafted with 5 × 10<sup>6</sup> tumor cells (HCT116, A549) or MYC/RAS double-transduced *Msh3*<sup>-/-</sup> or *Msh3*<sup>w/wt</sup> MEFs. The DNA-PKcs inhibitor KU60648 was dissolved in PBS at a final concentration of 6 mg/mL for xenograft application.

Upon the formation of palpable subcutaneous tumors, mice received intraperitoneal injections of either KU60648 (40 mg/kg) or PBS twice daily. Perpendicular tumor diameters were assessed daily by an external caliper, and tumor volumes were calculated by the modified ellipsoid formula [ $V = 1/2 (\text{length} \times \text{width}^2)$ ]. After 7 (double-transduced MEFs) or 14 (HCT116, A549) days of therapy, mice were sacrificed and subcutaneous tumors were resected and then fixed in 4% formalin overnight.

For further details, please refer to the Supplementary Methods.

### Disclosure of Potential Conflicts of Interest

L.C. Heukamp has received honoraria from the speakers' bureaus of Pfizer and Roche. H.C. Reinhardt has received honoraria from the speakers' bureau of Celgene. No potential conflicts of interest were disclosed by the other authors.

### Authors' Contributions

**Conception and design:** F. Dietlein, L. Thelen, M. Jokic, H.C. Reinhardt  
**Development of methodology:** F. Dietlein, L. Thelen, M. Jokic, R.D. Jachimowicz, L.C. Heukamp, H.C. Reinhardt

**Acquisition of data (provided animals, acquired and managed patients, provided facilities, etc.):** F. Dietlein, L. Thelen, R.D. Jachimowicz, L. Ivan, J. van Oers, W. Edelmann, L.C. Heukamp, H.C. Reinhardt

**Analysis and interpretation of data (e.g., statistical analysis, biostatistics, computational analysis):** F. Dietlein, L. Thelen, L. Ivan, U. Leeser, L.C. Heukamp, H.C. Reinhardt  
**Writing, review, and/or revision of the manuscript:** F. Dietlein, L. Thelen, L. Ivan, G. Knittel, J. van Oers, W. Edelmann, H.C. Reinhardt

**Administrative, technical, or material support (i.e., reporting or organizing data, constructing databases):** F. Dietlein, L. Thelen, G. Knittel, U. Leeser, L.C. Heukamp

### Grant Support

This work was supported by the Volkswagenstiftung (Lichtenberg Program, to H.C. Reinhardt), the Deutsche Forschungsgemeinschaft (KFO-286, RE2246/2-1, to H.C. Reinhardt), the Helmholtz-Gemeinschaft (Preclinical Comprehensive Cancer Center, to H.C. Reinhardt), the Ministry for Science and Technology, NRW (MIWT, 313-005-0910-0102, to H.C. Reinhardt), Deutsche Jose Carreras Stiftung (DJCLS-R12/26, to H.C. Reinhardt), Deutsche Krebshilfe (Mildred-Scheel-Doktorandenprogramm, 110770, to F. Dietlein), the KölnFortune program (to R.D. Jachimowicz and L. Ivan), and the NIH (CA76329 and CA93484, to W. Edelmann).

Received November 21, 2013; revised February 10, 2014; accepted February 14, 2014; published OnlineFirst February 20, 2014.

### REFERENCES

- Reinhardt HC, Yaffe MB. Phospho-Ser/Thr-binding domains: navigating the cell cycle and DNA damage response. *Nat Rev Mol Cell Biol* 2013;14:563–80.

2. Hoeijmakers JH. Genome maintenance mechanisms for preventing cancer. *Nature* 2001;411:366–74.
3. Hartlerode AJ, Scully R. Mechanisms of double-strand break repair in somatic mammalian cells. *Biochem J* 2009;423:157–68.
4. Lees-Miller SP, Meek K. Repair of DNA double strand breaks by non-homologous end joining. *Biochimie* 2003;85:1161–73.
5. Chapman JR, Taylor MR, Boulton SJ. Playing the end game: DNA double-strand break repair pathway choice. *Mol Cell* 2012;47:497–510.
6. Cimprich KA, Cortez D. ATR: an essential regulator of genome integrity. *Nat Rev Mol Cell Biol* 2008;9:616–27.
7. Sung P, Klein H. Mechanism of homologous recombination: mediators and helicases take on regulatory functions. *Nat Rev Mol Cell Biol* 2006;7:739–50.
8. Venkitaraman AR. Tracing the network connecting BRCA and Fanconi anaemia proteins. *Nat Rev Cancer* 2004;4:266–76.
9. Meindl A, Hellebrand H, Wiek C, Erven V, Wappenschmidt B, Niederacher D, et al. Germline mutations in breast and ovarian cancer pedigrees establish RAD51C as a human cancer susceptibility gene. *Nat Genet* 2010;42:410–4.
10. Bryant HE, Schultz N, Thomas HD, Parker KM, Flower D, Lopez E, et al. Specific killing of BRCA2-deficient tumours with inhibitors of poly(ADP-ribose) polymerase. *Nature* 2005;434:913–7.
11. Farmer H, McCabe N, Lord CJ, Tutt AN, Johnson DA, Richardson TB, et al. Targeting the DNA repair defect in BRCA mutant cells as a therapeutic strategy. *Nature* 2005;434:917–21.
12. Gurley KE, Kemp CJ. Synthetic lethality between mutation in Atm and DNA-PK(cs) during murine embryogenesis. *Curr Biol* 2001;11:191–4.
13. Jiang H, Reinhardt HC, Bartkova J, Tommiska J, Blomqvist C, Nevanlinna H, et al. The combined status of ATM and p53 link tumor development with therapeutic response. *Genes Dev* 2009;23:1895–909.
14. Riabinska A, Daheim M, Herter-Sprie GS, Winkler J, Fritz C, Hallek M, et al. Therapeutic targeting of a robust non-oncogene addiction to PRKDC in ATM-defective tumors. *Sci Transl Med* 2013;5:189ra78.
15. Munck JM, Batey MA, Zhao Y, Jenkins H, Richardson CJ, Cano C, et al. Chemosensitization of cancer cells by KU-0060648, a dual inhibitor of DNA-PK and PI-3K. *Mol Cancer Ther* 2012;11:1789–98.
16. Barretina J, Caponigro G, Stransky N, Venkatesan K, Margolin AA, Kim S, et al. The Cancer Cell Line Encyclopedia enables predictive modelling of anticancer drug sensitivity. *Nature* 2012;483:603–7.
17. Forbes SA, Bhamra G, Bamford S, Dawson E, Kok C, Clements J, et al. The Catalogue of Somatic Mutations in Cancer (COSMIC). *Curr Protoc Hum Genet* 2008;Chapter 10:Unit 10.1.
18. Garnett MJ, Edelman EJ, Heidorn SJ, Greenman CD, Dastur A, Lau KW, et al. Systematic identification of genomic markers of drug sensitivity in cancer cells. *Nature* 2012;483:570–5.
19. Malchers F, Dietlein F, Schottel J, Lu X, Nogova L, Albus K, et al. Cell-autonomous and non-cell-autonomous mechanisms of transformation by amplified FGFR1 in lung cancer. *Cancer Discov* 2014;4:246–57.
20. Dietlein F, Eschner W. Inferring primary tumor sites from mutation spectra: a meta-analysis of histology-specific aberrations in cancer-derived cell lines. *Hum Mol Genet* 2014;23:1527–37.
21. Daniel JA, Santos MA, Wang Z, Zang C, Schwab KR, Jankovic M, et al. PTIP promotes chromatin changes critical for immunoglobulin class switch recombination. *Science* 2010;329:917–23.
22. Wang X, Takenaka K, Takeda S. PTIP promotes DNA double-strand break repair through homologous recombination. *Genes Cells*. 2010 Jan 19. [Epub ahead of print].
23. Ashburner M, Ball CA, Blake JA, Botstein D, Butler H, Cherry JM, et al. Gene ontology: tool for the unification of biology. The Gene Ontology Consortium. *Nat Genet* 2000;25:25–9.
24. Risinger JI, Umar A, Boyd J, Berchuck A, Kunkel TA, Barrett JC. Mutation of MSH3 in endometrial cancer and evidence for its functional role in heteroduplex repair. *Nat Genet* 1996;14:102–5.
25. Park JM, Huang S, Tougeron D, Simicope FA. MSH3 mismatch repair protein regulates sensitivity to cytotoxic drugs and a histone deacetylase inhibitor in human colon carcinoma cells. *PLoS ONE* 2013;8:e65369.
26. Haugen AC, Goel A, Yamada K, Marra G, Nguyen TP, Nagasaka T, et al. Genetic instability caused by loss of MutS homologue 3 in human colorectal cancer. *Cancer Res* 2008;68:8465–72.
27. Plaschke J, Kruger S, Jeske B, Theissig F, Kreuz FR, Pistorius S, et al. Loss of MSH3 protein expression is frequent in MLH1-deficient colorectal cancer and is associated with disease progression. *Cancer Res* 2004;64:864–70.
28. San Filippo J, Sung P, Klein H. Mechanism of eukaryotic homologous recombination. *Annu Rev Biochem* 2008;77:229–57.
29. Bartkova J, Rezaei N, Lintont M, Karakaidos P, Kletsas D, Issaeva N, et al. Oncogene-induced senescence is part of the tumorigenesis barrier imposed by DNA damage checkpoints. *Nature* 2006;444:633–7.
30. Di Micco R, Fumagalli M, Cicalese A, Piccinin S, Gasparini P, Luise C, et al. Oncogene-induced senescence is a DNA damage response triggered by DNA hyper-replication. *Nature* 2006;444:638–42.
31. Gorgoulis VG, Vassiliou LV, Karakaidos P, Zacharatos P, Kotsinas A, Liloglou T, et al. Activation of the DNA damage checkpoint and genomic instability in human precancerous lesions. *Nature* 2005;434:907–13.
32. Bartkova J, Horejsi Z, Koed K, Kramer A, Tort F, Zieger K, et al. DNA damage response as a candidate anti-cancer barrier in early human tumorigenesis. *Nature* 2005;434:864–70.
33. Loeb LA, Loeb KR, Anderson JP. Multiple mutations and cancer. *Proc Natl Acad Sci U S A* 2003;100:776–81.
34. Loeb LA, Bielas JH, Beckman RA. Cancers exhibit a mutator phenotype: clinical implications. *Cancer Res* 2008;68:3551–7.
35. Jiricny J. The multifaceted mismatch-repair system. *Nat Rev Mol Cell Biol* 2006;7:335–46.
36. Network TCGAR. Integrated genomic analyses of ovarian carcinoma. *Nature* 2011;474:609–15.
37. Reinhardt HC, Jiang H, Hemann MT, Yaffe MB. Exploiting synthetic lethal interactions for targeted cancer therapy. *Cell Cycle* 2009;8:3112–9.
38. Fallahi-Sichani M, Honarnejad S, Heiser LM, Gray JW, Sorger PK. Metrics other than potency reveal systematic variation in responses to cancer drugs. *Nat Chem Biol* 2013;9:708–14.
39. Sugawara N, Ira G, Haber JE. DNA length dependence of the single-strand annealing pathway and the role of *Saccharomyces cerevisiae* RAD59 in double-strand break repair. *Mol Cell Biol* 2000;20:5300–9.
40. Sugawara N, Paques F, Colaiacovo M, Haber JE. Role of *Saccharomyces cerevisiae* Msh2 and Msh3 repair proteins in double-strand break-induced recombination. *Proc Natl Acad Sci U S A* 1997;94:9214–9.
41. Lyndaker AM, Alani E. A tale of tails: insights into the coordination of 3' end processing during homologous recombination. *BioEssays* 2009;31:315–21.
42. Zhang Y, Rohde LH, Wu H. Involvement of nucleotide excision and mismatch repair mechanisms in double strand break repair. *Curr Genomics* 2009;10:250–8.
43. van Oers JM, Edwards Y, Chahwan R, Zhang W, Smith C, Pechuan X, et al. The MutSbeta complex is a modulator of p53-driven tumorigenesis through its functions in both DNA double-strand break repair and mismatch repair. *Oncogene*. 2013 Sep 9. [Epub ahead of print].
44. Toledo F, Wahl GM. Regulating the p53 pathway: *in vitro* hypotheses, *in vivo* veritas. *Nat Rev Cancer* 2006;6:909–23.
45. Lord CJ, Ashworth A. The DNA damage response and cancer therapy. *Nature* 2012;481:287–94.
46. Cancer Genome Atlas N. Comprehensive molecular characterization of human colon and rectal cancer. *Nature* 2012;487:330–7.
47. Sos ML, Dietlein F, Peifer M, Schottel J, Balke-Want H, Muller C, et al. A framework for identification of actionable cancer genome dependencies in small cell lung cancer. *Proc Natl Acad Sci U S A* 2012;109:17034–9.
48. Frommolt P, Thomas RK. Standardized high-throughput evaluation of cell-based compound screens. *BMC Bioinformatics* 2008;9:475.
49. Adzhubei IA, Schmidt S, Peshkin L, Ramensky VE, Gerasimova A, Bork P, et al. A method and server for predicting damaging missense mutations. *Nat Methods* 2010;7:248–9.
50. Reinhardt HC, Hasskamp P, Schmedding I, Morandell S, van Vuugt MA, Wang X, et al. DNA damage activates a spatially distinct late cytoplasmic cell-cycle checkpoint network controlled by MK2-mediated RNA stabilization. *Mol Cell* 2010;40:34–49.